J|A|C|S
ARTICLES

Published on Web 09/15/2009

In Situ and Ex Situ Studies of Platinum Nanocrystals: Growth and Evolution in Solution

Soshan Cheong,[†,‡] John Watt,[†,‡] Bridget Ingham,[‡,§] Michael F. Toney,[⊥] and Richard D. Tilley*,[†,‡]

School of Chemical and Physical Sciences and The MacDiarmid Institute for Advanced Materials and Nanotechnology, Victoria University of Wellington, Wellington 6012, New Zealand, Industrial Research Limited, P.O. Box 31-310, Lower Hutt 5040, New Zealand, and Stanford Synchrotron Radiation Lightsource, SLAC National Accelerator Laboratory, Menlo Park, California 94025

Received August 3, 2009; E-mail: richard.tilley@vuw.ac.nz

Abstract: In situ studies on the growth and evolution of platinum nanocrystals in solution were carried out using synchrotron-based X-ray diffraction (XRD) techniques. Ex situ low- and high-resolution transmission electron microscopy (TEM) were used to investigate the nanocrystal morphologies through the different growth stages. In a reaction with low precursor concentration, both XRD and TEM results show that growth occurs at a relatively slow rate and yields faceted morphologies, which are characteristic of a thermodynamically controlled regime. In contrast, the platinum nanocrystals in the high-concentration reaction form branched structures and grow at much greater rates under a kinetically controlled regime. Additionally the growth mechanism of the high-concentration reaction involves a morphology transformation from octapod-like shapes to porous nanostructures, which is brought about by a novel mechanism involving selective growth and etching processes that occur simultaneously and at comparable rates.

Introduction

Platinum nanostructures have been receiving a great deal of attention because of their unique catalytic properties and a wide variety of economically driven applications in catalysis and electrocatalysis.[1−4] It has been established that in a finely divided state, the catalytic activity and selectivity of platinum for a particular reaction are dependent on the particle size and shape and on the crystallographic plane that terminates the particle surface.[5−8] For these reasons, research efforts have been devoted to size reduction for maximizing the surface-to-volume ratio, and to morphology control for improving selectivity.

In solution-phase synthesis, platinum nanoparticles of spherical or near-spherical structures and polyhedra enclosed by $\{100\}$ and/or $\{111\}$ facets are the most commonly reported.[9−11] Recent studies have also shown the capability to produce unconventional structures such as nanoparticles bound by high-index facets,[7] nanowires,[12] multiarmed, and porous nanostructures.[13−16]

Understanding the nanoparticle growth mechanism and the kinetics governing growth provides an essential means to predict the conditions needed for controlled synthesis to tailor the desired properties. Recent reviews in the literature have profoundly discussed the importance and challenges in understanding and controlling nanoparticle growth in achieving well-defined properties.[17−20] The tested strategies to manipulate growth kinetics, particularly those of metal nanocrystals, include selective capping by suitable stabilizing agents,[21,22] controlling

---

[†] School of Chemical and Physical Sciences, Victoria University of Wellington.

[‡] The MacDiarmid Institute for Advanced Materials and Nanotechnology, Victoria University of Wellington.

[§] Industrial Research Limited.

[⊥] Stanford Synchrotron Radiation Lightsource.

(1) Somorjai, G. A.; Blakely, D. W. *Nature* **1975**, *258*, 580–583.
(2) Williams, K. R.; Burstein, G. T. *Catal. Today* **1997**, *38*, 401–410.
(3) Bell, A. T. *Science* **2003**, *299*, 1688–1691.
(4) Chen, J.; Lim, B.; Lee, E. P.; Xia, Y. *Nano Today* **2009**, *4*, 81–95.
(5) Falicov, L. M.; Somorjai, G. A. *Proc. Natl. Acad. Sci. U.S.A.* **1985**, *82*, 2207–2211.
(6) Narayanan, R.; El-Sayed, M. A. *J. Am. Chem. Soc.* **2004**, *126*, 7194–7195.
(7) Tian, N.; Zhou, Z.-Y.; Sun, S.-G.; Ding, Y.; Wang, Z. L. *Science* **2007**, *316*, 732–735.
(8) Bratlie, K. M.; Lee, H.; Komvopoulos, K.; Yang, P.; Somorjai, G. A. *Nano Lett.* **2007**, *7*, 3097–3101.
(9) Ahmandi, T. S.; Wang, Z. L.; Green, T. C.; Henglein, A.; El-Sayed, M. A. *Science* **1996**, *272*, 1924–1926.
(10) Miyazaki, A.; Nakano, Y. *Langmuir* **2000**, *16*, 7109–7111.
(11) Song, H.; Kim, F.; Connor, S.; Somorjai, G. A.; Yang, P. *J. Phys. Chem. B* **2005**, *109*, 188–193.
(12) Fenske, D.; Borchert, H.; Kehres, J.; Kroger, R.; Parisi, J.; Kolny-Olesiak, J. *Langmuir* **2008**, *24*, 9011–9016.
(13) Mahmoud, M. A.; Tabor, C. E.; Ding, Y.; Wang, Z. L.; El-Sayed, M. A. *J. Am. Chem. Soc.* **2008**, *130*, 4590–4591.
(14) Teng, X.; Liang, X.; Maksimuk, S.; Yang, H. *Small* **2006**, *2*, 249–253.
(15) Zhong, X.; Feng, Y.; Lieberwirth, I.; Knoll, W. *Chem. Mater.* **2006**, *18*, 2468–2471.
(16) Ren, J.; Tilley, R. D. *Small* **2007**, *3*, 1508–1512.
(17) Burda, C.; Chen, X.; Narayanan, R.; El-Sayed, M. A. *Chem. Rev.* **2005**, *105*, 1025–1102.
(18) Park, J.; Joo, J.; Kwon, S. G.; Jang, Y.; Hyeon, T. *Angew. Chem., Int. Ed.* **2007**, *46*, 4630–4660.
(19) Pileni, M.-P. *J. Phys. Chem. C* **2007**, *111*, 9019–9038.
(20) Xia, Y.; Xiong, Y.; Lim, B.; Skrabalak, S. E. *Angew. Chem., Int. Ed.* **2009**, *48*, 60–103.
(21) Petroski, J. M.; Wang, Z. L.; Green, T. C.; El-Sayed, M. A. *J. Phys. Chem. B* **1998**, *102*, 3316–3320.
(22) Puntes, V. F.; Krishnan, K. M.; Alivisatos, A. P. *Science* **2001**, *291*, 2115–2117.

10.1021/ja9065688 CCC: $40.75

the rate of decomposition or reduction of metal precursors,[23,24] and deliberate introduction of an etching mechanism.[25,26] The understanding of these concepts has mainly been developed through ex situ studies by quenching the growth process at different reaction times and examining the intermediate products using X-ray diffraction (XRD), transmission electron microscopy (TEM), and spectroscopy techniques. Kinetic studies based on an in situ, or real time, approach are relatively recent and have mainly concentrated on nanocrystal growth in terms of crystallite size changes but not considered the shape evolution during the growth process.[27−29]

In this paper, we present results obtained from both in situ and ex situ studies of the growth of platinum nanocrystals in solution. Synchrotron-based XRD was employed to study the growth of platinum nanocrystals in real time and to provide a direct assessment of the crystallinity, nanocrystal concentration, and crystallite size of the product. TEM was then used to investigate the nanoparticle morphology at different growth stages. For reactions with different precursor concentrations, the platinum nanocrystal growth and shape evolution are shown to be governed by different growth kinetics. By combining the results and observations from both in situ and ex situ studies, the different growth mechanisms associated with thermodynamic and kinetic growth regimes are elucidated and discussed. We believe the understanding that we develop of the growth mechanism of branched and porous nanostructures is of fundamental importance and can be generalized to other face-centered-cubic (fcc) metals.

Experimental Section

Materials. All reagents were used as received without further purification. Platinum(II) acetylacetonate (Pt(acac)$_2$), absolute toluene, and absolute methanol were purchased from Sigma-Aldrich. Oleylamine (>70%) was purchased from Fluka.

Precursor Solution. All precursor solutions were prepared at room temperature in a fume cupboard. In a typical reaction, the high-concentration precursor solution was prepared by dissolving 0.05 mmol (0.0196 g) of Pt(acac)$_2$ in 1 mL of toluene, making a 0.05 M solution, to which 0.5 mmol (0.165 mL) of oleylamine was added. For reaction with low precursor concentration, 0.1 mL of the 0.05 M solution was diluted by adding toluene to make up 1 mL of solution, giving 0.005 M. The mole ratio of oleylamine to Pt(II) was 10:1 for both precursor solutions.

Reaction Cell. For the in situ XRD, the reaction cell was made of stainless steel and comprised two parts mounted together by screws. (A photo of the reaction cell is shown in Figure S1 in the Supporting Information.) The bottom piece was the reaction vessel where reactions took place, whereas the top was a cylindrical chamber equipped with a three-way valve to allow for control of reaction atmosphere. The two pieces together gave the reaction cell an internal volume of about 300 mm^3. The disk-shaped reaction vessel was 1 mm thick, with polyimide (Kapton) windows on both flat faces. It had an opening on the top to allow for transfer of fluids. This was also where the top piece was mounted.

In Situ Synchrotron XRD. Synchrotron XRD measurements were conducted at the Stanford Synchrotron Radiation Lightsource (SSRL) at beamline 7−2. For each experiment, about 0.05 mL of the precursor solution was injected to the reaction vessel. The cell was then closed by mounting the reaction vessel and the valve-chamber together. Using the valve, the cell was flushed through with H$_2$, before being filled to 200 kPa H$_2$. At the start of an experiment, the reaction cell was inserted into a ceramic heating block fitted with a temperature controller and a thermocouple. It usually took less than 5 min to heat the ceramic block from room temperature to 70 °C, which was the temperature maintained for the duration of the experiment. The XRD measurements were conducted using radiation of $\lambda = 0.775$ Å with a point detector geometry using 1 mrad ($\approx 0.057°$) Soller slits. Diffractograms were collected over the Pt(111) and Pt(200) peaks between 2θ values of 18 and 24°, using step scans of 0.05°/step and a counting time of 2−3 s/step. Each scan took 5−10 min. Scans were taken repeatedly during the growth of the Pt(111) and Pt(200) diffraction peaks, for 500 min (~8.5 h).

TEM Characterization. Products collected from the experiments were purified by addition of methanol to flocculate and precipitate the nanocrystals, which were collected by centrifugation. The samples for TEM studies were prepared by resuspending the precipitate in toluene. One drop of the toluene suspension was put onto a carbon-supported TEM grid and allowed to evaporate under ambient conditions. The TEM images and electron diffraction patterns were taken on a JEOL 2010 operated at an acceleration voltage of 200 keV.

Results

In Situ X-ray Diffraction. Precursor concentration has been shown to strongly dictate the final morphology of platinum nanocrystals.[16,30] In order to investigate nanocrystal growth under the influence of precursor concentration, synchrotron-based in situ XRD experiments were conducted. The synthesis involved thermal decomposition of a platinum precursor in a reaction vessel in the presence of a stabilizing agent, under a hydrogen atmosphere. Two precursor concentrations were employed in this study, 0.005 and 0.05 M Pt(acac)$_2$ in toluene, and are labeled as low conc. and high conc., respectively.

Upon completion of both experiments a colloidal solution was obtained and there was no accumulation of the nanoparticles on the windows of the cell and so the Pt(111) and Pt(200) signals obtained came from the nanoparticles in the solution.

Figure 1 shows the results obtained from the XRD experiments. In situ XRD plots after subtraction of the solution scattering background for both low- and high-concentration experiments are shown in Figure 1A. No peaks are initially observed for both reactions (less than 60 min), most likely due to the initial crystallites being too small to be observed and/or there being a short induction time before nanoparticle nucleation. As the reactions proceed, small peaks corresponding to Pt(111) and Pt(200) begin to emerge and progressively grow over time. The initial peaks are generally broad, especially when they first appear, indicating the formation of small crystallites. As the reaction proceeds, the peak areas increase, indicating an increase in the concentration of nanocrystalline platinum ([Pt$_{NC}$]) within the (constant) diffracting volume, and the peaks get narrower, indicating an increase in the average crystallite size.

The lattice parameters were calculated from the peak positions and the difference between the calculated and the bulk lattice values, Δd, was determined. The difference, Δd, was calculated as -0.002 ± 0.001 Å and -0.004 ± 0.001 Å for the low- and high-concentration reactions, respectively. The calculated lattice parameters were thus close to the bulk showing little or no strain

---

(23) Herricks, T.; Chen, J.; Xia, Y. *Nano Lett.* **2004**, *4*, 2367–2371.
(24) Teng, X.; Yang, H. *Nano Lett.* **2005**, *5*, 885–891.
(25) Rodriguez-Fernandez, J.; Perez-Juste, J.; Mulvaney, P.; Liz-Marzan, L. M. *J. Phys. Chem. B* **2005**, *109*, 14257–14261.
(26) Xiong, Y.; Cai, H.; Wiley, B. J.; Wang, J.; Kim, M. J.; Xia, Y. *J. Am. Chem. Soc.* **2007**, *129*, 3665–3675.
(27) Qu, L.; Yu, W. W.; Peng, X. *Nano Lett.* **2004**, *4*, 465–469.
(28) Viswanatha, R.; Amenitsch, H.; Sarma, D. D. *J. Am. Chem. Soc.* **2007**, *129*, 4470–4475.
(29) Biswas, K.; Varghese, N.; Rao, C. N. R. *Small* **2008**, *4*, 649–655.
(30) Ren, J.; Tilley, R. D. *J. Am. Chem. Soc.* **2007**, *129*, 3287–3291.

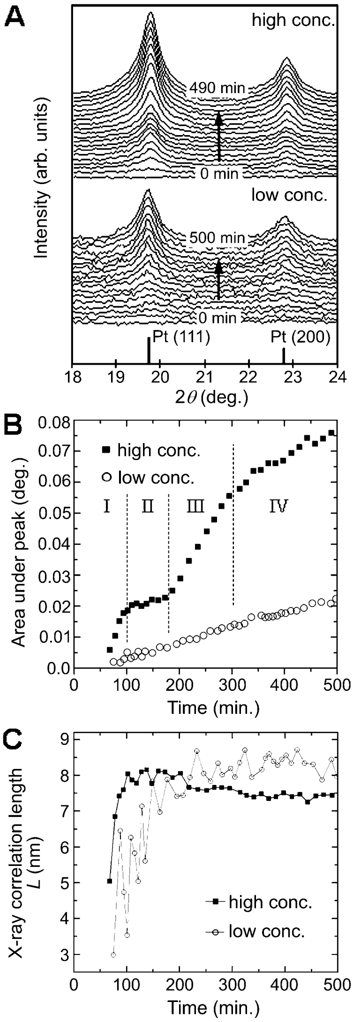

Figure 1. Time-resolved XRD results obtained for both low- and high-concentration reactions. (A) In situ XRD plots; the position of the (111) and (200) reflections for bulk fcc platinum is shown by the lines at bottom of plot; (B) time evolution of area under the Pt(111) peak. I−IV denote the growth stages of the high-concentration reaction; (C) evolution of X-ray correlation length (*L*) calculated from fwhm of Pt(111) peak. The resolution (upper) limit is about 20 nm.

within the nanocrystal domains, which is expected given the relatively large crystallite sizes. A plot of Δd against time for the low- and high-concentration reactions are shown in Figures S2 and S3 in the Supporting Information, respectively. Within the error bars, there are no systematic trends.

Figure 1B shows the plot of area under the Pt(111) peak against time for both low- and high-concentration reactions. The area integrated under the Pt(200) peak has the same profile as that obtained from the Pt(111) peak, and both profiles are identical after being normalized to the final maximum value. Figures S4 and S5 in the Supporting Information show the time-dependent normalized peak area plot for both experiments. As shown in Figure 1B, the peak area plot for the low-concentration reaction increases approximately linearly over the course of experiment, indicating a continuous and almost constant increase of [Pt_{NC}]. For the high-concentration reaction, the peak area plot is more complex and can be divided into four stages based on the slope of the growth plot. For the first ∼60−100 min of growth, denoted as Stage I, the peak area increases rapidly and linearly, with a slope that is ten times greater than that of the low-concentration plot. This indicates a 10-fold increase in the growth rate of [Pt_{NC}] in the high-concentration reaction compared to that in the low-concentration reaction. Remarkably, between ∼100 and 180 min, denoted as Stage II, the peak area remains almost constant, which shows almost no growth in [Pt_{NC}]. From ∼180−300 min, denoted as Stage III, the peak area resumes with a more rapid increase; the gradient is ∼60% of that observed in Stage I, but is still much larger than that for the low-concentration reaction and thus [Pt_{NC}] increases rapidly again. From around 300 min, denoted as Stage IV, the slope of the area plot decreases slightly, with a gradient of about 1/3 of that in the previous stage (Stage III), which is indicative of a slower increase in [Pt_{NC}].

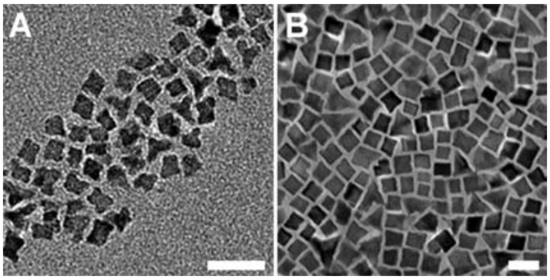

Figure 2. TEM images of platinum nanoparticles from low concentration reactions after (A) 80 and (B) 400 min. Both scale bars are 20 nm.

Information on the crystallite size was obtained by calculating the X-ray correlation length (*L*) from the full width at half-maximum (fwhm) of the Pt(111) and Pt(200) peaks using the Scherrer equation.[31] The *L* value calculated from the fwhm of Pt(200) is identical to that calculated from the fwhm of Pt(111). Figures S6 and S7 in the Supporting Information show the plot of *L* determined from fwhm of Pt(111) and Pt(200) peaks for both experiments. The relatively broad peak widths observed were a result of the crystallite size rather than the angular resolution limit of the detector (which was about 0.1°, corresponding to a maximum size of 20 nm). In Figure 1C, *L* calculated from the fwhm of Pt(111) peak is plotted against time for both low- and high-concentration reactions. The X-ray correlation length for the low-concentration reaction increases from 3 nm at 75 min to 8.6 nm at 230 min. It then remains almost constant at about 8.4 ± 0.3 nm for the remainder of the reaction. For the high-concentration reaction, *L* increases during Stage I from initially ∼5 nm to ∼8.2 nm at 100 min. During Stage II, *L* remains almost constant between 100 and 180 min at 8.0 ± 0.2 nm. Interestingly, during Stage III, 180−300 min, *L* actually decreases from 8.1 to 7.6 nm, differing markedly from the low-concentration reaction. After 300 min, *L* continues to decrease gradually and is calculated to be ∼7.4 nm at the end of Stage IV.

Transmission Electron Microscopy. To better understand the growth mechanisms of the low- and high-concentration reactions, we carried out a series of off-line, ex situ, experiments with each reaction quenched after certain growth stages. Products collected from both in situ and ex situ experiments were characterized using TEM. The reaction times for the off-line experiments were selected on the basis of interesting regions in the XRD data.

Figure 2 shows the TEM images of platinum nanoparticles obtained from the low-concentration reaction. As shown in Figure 2A, the product collected from a reaction quenched at

---

(31) Borchert, H.; Shevchenko, E. V.; Robert, A.; Mekis, I.; Kornowski, A.; Grubel, G.; Weller, H. *Langmuir* **2005**, *21*, 1931–1936.

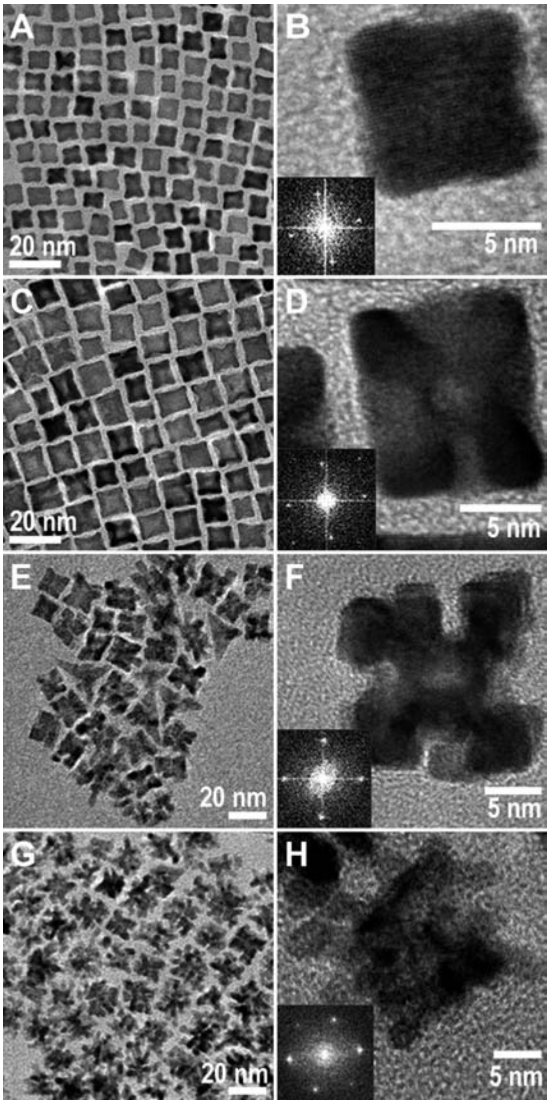

Figure 3. TEM images of platinum nanoparticles obtained from high-concentration reactions of (A, B) 75, (C, D) 120, (E, F) 240, and (G, H) 500 min. Insets in Figures B, D, F, and H show the power spectra (Fast Fourier Transform) of the respective images.

80 min comprises faceted nanoparticles of irregular shapes, with particle sizes measured in the range of 6 ± 2 nm. High-resolution TEM (HRTEM) imaging shows that some of these nanoparticles are twinned while most are single crystal. An HRTEM image is shown in Figure S8 in the Supporting Information. The ratio of twinned to single crystal is ∼1:6. The size range is thus consistent with the X-ray correlation length shown in Figure 1C. Figure 2B shows the TEM image of the platinum nanoparticles collected after 400 min. These nanoparticles display similar morphologies to those observed in Figure 2A, but are of bigger size range, averaging 11 ± 3 nm (again consistent with Figure 1C).

Images A, C, E, and G in Figure 3 show the TEM images of platinum nanoparticles collected from the high-precursor concentration reaction at 75, 120, 240, and 500 min, corresponding to Stages I−IV, respectively. It can be clearly observed that the nanoparticle morphology is highly time-dependent. It is also observed that the nanoparticles are single crystals at all four times, as evident in images B, D, F, and H in Figure 3.

As shown in Figure 3A, the platinum nanocrystals formed at 75 min, the middle of Stage I, adopt a nearly cubic morphology and have an average size of 6.5 ± 0.6 nm. Figure 3B shows the TEM image of a typical nanocrystal, with the corresponding power spectrum (Fast Fourier Transform) of the image shown in the inset. The power spectrum indicates that the platinum nanocrystal is a single crystal and can be indexed as being projected along a $\langle 100\rangle$ zone axis. On the basis of this projection, the exposed flat faces of the nanocrystal can be identified as the $\{100\}$ facets. However, differing from a nanocube that has sharp corners/vertices, the observed nanocrystal has protruded and rounded corners appearing as short arms projecting along the $\langle 111\rangle$ directions. Generally, nanoparticles with eight arms/pods are known as octapods.[23,30] Because of the short arms displayed by the platinum nanocrystals observed here, they are described as quasi-octapods.

Figure 3C shows the platinum nanocrystals collected at 120 min, the middle of Stage II. These nanocrystals are larger in size, at an average of 11.2 ± 0.6 nm, and have the same $\langle 100\rangle$ orientation as displayed by the quasi-octapods. Figure 3D shows the TEM image of a typical nanocrystal obtained during this stage, with the inset showing the corresponding power spectrum, indicating again a single-crystalline structure and a $\langle 100\rangle$ orientation. Close examination on the TEM images reveals that these nanocrystals do not appear exactly the same as the quasi-octapods. On the basis of observations in the TEM, the nanocrystals at 120 min have thinner cross sections toward the center of the $\{100\}$ faces, indicative of etching. For this reason and from the growth mechanism discussed in the next section, we describe these nanocrystals as etched-octapods. Both the quasi- and the etched-octapods tend to assemble into cubic packing when the nanoparticle suspension dries on a TEM grid.

Figure 3E shows the platinum nanocrystals obtained at 240 min, middle of Stage III. The nanocrystals comprise a mixture of etched-octapods and porous nanostructures, in a ratio of ∼1:3. The latter is also known as porous platinum[14] and is described as porous nanocrystal. A typical porous nanocrystal is shown in Figure 3F, with the power spectrum of the image of the whole particle shown in the inset, indicating single crystallinity and an orientation along a $\langle 100\rangle$ zone axis. The porous nanocrystals are typically 19 ± 2 nm in size. As shown in Figure 3G, the platinum nanocrystals obtained at 500 min, late Stage IV, are almost exclusively porous nanocrystals. With an average size of 24 ± 3 nm, these porous nanocrystals are generally larger than the same species obtained at 240 min. Figure 3H shows a typical porous nanocrystal obtained at this stage. As indicated by the corresponding power spectrum (inset) the nanoparticle is a single crystal being viewed down on a $\langle 110\rangle$ zone axis. The HRTEM images of the nanoparticles in Figures 3F and 3H are included in the Supporting Information, as Figures S9 and S10, showing clearly the lattice fringes across the entire nanocrystals indicating that they are single crystal. Therefore, TEM data show that the platinum nanoparticles in the high-concentration reaction at 75−500 min are single-crystalline structures that display highly time-dependent morphologies.

Discussion

The in situ XRD data and ex situ TEM images described above show that platinum nanoparticles prepared from precursor solutions of low and high concentrations grow at different rates and form different morphologies.

Growth Mechanism: Low-Concentration Reaction (0.005 M Pt(acac)$_2$). The peak area plot in Figure 1B indicates the growth rate of $[\mathrm{Pt_{NC}}]$ is much slower for the low-concentration reaction, compared to that for the high-concentration reaction.

TEM evidence, shown in Figure 2A, indicates the formation of faceted and nonbranched morphologies from an early growth stage. Slow nanocrystal growth and formation of nonbranched morphologies have been shown to be characteristic of growth in a thermodynamically controlled growth regime.[20,32,33]

With the low precursor concentration, a low solution concentration of free platinum atoms is produced, resulting in relatively slow nanocrystal growth as indicated by the XRD result in Figure 1B. TEM observation of nanoparticles from the different reaction times in Figure 2 shows that nanoparticle morphologies are maintained throughout the reaction. Nanoparticles of similar morphologies were also obtained from a reaction of 900 min (15 h), as shown in Figure S11 in the Supporting Information. Nanocrystal growth in the low-concentration reaction therefore occurs under thermodynamic control via a slow, nearly layer-by-layer monomer addition onto the crystallite faces to yield stable morphologies.

The average particle size measured on TEM images are in good agreement with the calculated L. This gives a good indication that the nanocrystals as observed in the TEM are representative of the products obtained.

Growth Mechanism: High-Concentration Reaction (0.05 M Pt(acac)$_2$). The peak area plot in Figure 1B indicates that the growth of the nanocrystals in the high-concentration reaction occurs in Stages I to IV.

Stage I: Formation of Quasi-Octapods. The XRD data shows that the increase of [Pt$_{NC}$] during Stage I is rapid and there is fast growth of nanocrystals. A fast growth rate has been associated with kinetically controlled growth, which often leads to a complex growth pattern and nanocrystals having branched morphologies.[32] Interpretation from TEM imaging suggests that the platinum nanocrystals in the high-concentration reaction nucleate and grow into quasi-octapods during this stage. As described earlier, a quasi-octapod has eight short arms growing along the $\langle 111 \rangle$ directions from the eight corners of a cubic core with $\{100\}$ terminating facets. For fcc metals such as gold and platinum, a single-crystalline nanocrystal often originates from a cuboctahedral nucleus or seed that is enclosed by six $\{100\}$ facets and eight $\{111\}$ facets.[34,35] The observed quasi-octapods are believed to be a result of faster growth on the $\{111\}$ facets than on the $\{100\}$ facets, giving rise to the short arms along the $\langle 111 \rangle$ directions.

Stage II: Quasi-Octapods → Etched-Octapods. As shown in panels B and C in Figure 1, there is little change in the total amount of platinum atoms in the nanocrystals ([Pt$_{NC}$]) in Stage II. TEM images show that the arms of the quasi-octapods have grown by ~2.5 nm along the $\langle 111 \rangle$ directions, whereas the cross section toward the center of the $\{100\}$ facets have been reduced by 1−2 nm (Figure 3A−D). The growth on the quasi-octapods thus takes place over the arms along the $\langle 111 \rangle$ directions, whereas etching has occurred on the $\{100\}$ facets, leading to the formation of etched-octapods.

By correlating the observations in XRD and TEM, it can be seen that the increase in [Pt$_{NC}$] due to nanocrystal growth is balanced by the loss of redissolved platinum atoms from the nanocrystals as a consequence of etching; hence the [Pt$_{NC}$] peak area remains constant over this growth stage. Similarly, the near-constant X-ray correlation length as observed in Figure 1C is evidence of an increase and decrease in the crystallite size that effectively average out to no change. This result is highly interesting and to the best of our knowledge the first observation of both growth and etching processes occurring selectively, simultaneously, and at comparable rates for metal nanocrystals.

As further note, Figure S5 in the Supporting Information shows that the ratio of Pt(111):Pt (200) peak areas remains approximately the same throughout the reaction. The identical peak areas is expected as the Pt(111) and Pt(200) signals were resulted from the nanoparticles in motion solution and so no specific crystallographic orientation is observed.

Stage III: Etched-Octapods → Porous Nanocrystals. The relatively rapid increase in [Pt$_{NC}$] in Stage III is similar to that observed in Stage I, which indicates that the growth at this stage again occurs under kinetic control. However, the slight decrease in L suggests an unconventional type of growth. As can be observed in the TEM (Figures 3C − 3F), the cross sections toward the center of the (100) faces of the porous nanocrystals at 240 min are noticeably thinner (Figure 3F) as compared with those of the etched-octapods. A significant change in the particle morphology is gradually taking place, which is characterized by etching of much of the central core and the formation of more branches. These changes lead to an increase in porosity of the nanocrystals. As the nanocrystals become increasingly porous, the average size of the single-crystalline domains, and hence L, decreases.

Stage IV: Growth of Porous Nanocrystals. Both XRD and TEM results suggest that the porous nanocrystals continue to grow but at a relatively slower rate compared to stages I and III. Ex situ TEM was conducted for nanoparticles obtained after an extended reaction time of 900 min (15 h), and the resulting platinum nanoparticles were also porous and highly branched structures, as shown in Figure S12 in the Supporting Information. Apart from a few nanoparticles greater than 50 nm, the average nanoparticle size remains approximately the same as that observed in Figure 3G, in Stage IV. The slow growth from Stage IV onward can be understood as a result of monomer depletion in the solution.

It is interesting to note that at Stage I, the TEM average nanocrystal size (6.5 nm) agrees well with the X-ray correlation length L (6 nm), confirming the single crystal nature of the quasi-octapod nanoparticles. In contrast, in Stages II−IV, L is noticeably smaller than the TEM average nanocrystal size: through Stages II−IV, L decreases slightly from 8.0 to 7.4 nm, whereas the TEM nanocrystal size increases from 11 to 19 and 24 nm. Thus the variance between the L and the nanoparticle size obtained from the TEM images is a useful measure of nanoparticle porosity.

To summarize the high-concentration discussion, we have observed a growth mechanism of multiply branched or porous platinum nanocrystals that is under kinetic control and involves rapid growth and selective etching. The scheme in Figure 4 illustrates the proposed growth mechanism from Stage I to III.

Etching Process in the High-Concentration Reaction. During the growth of the platinum nanocrystals, one point of particular interest is Stage II, where simultaneous selective growth and etching take place at comparable rates, leading to shape transformation but no overall nanocrystal growth.

In terms of a possible etchant species, a mixture of surfactant, solvent, and precursor are present in solution-phase synthesis. The main etchants for noble metals are halide ions and oxygen

---

(32) Yin, Y.; Alivisatos, A. P. *Nature* **2005**, *437*, 664–670.

(33) Berhault, G.; Bausach, M.; Bisson, L.; Becerra, L.; Thomazeau, C.; Uzio, D. *J. Phys. Chem. C* **2007**, *111*, 5915–5925.

(34) Wang, Z. L. *J. Phys. Chem. B* **2000**, *104*, 1153–1175.

(35) Maksimuk, S.; Teng, X.; Yang, H. *J. Phys. Chem. C* **2007**, *111*, 14312–14319.

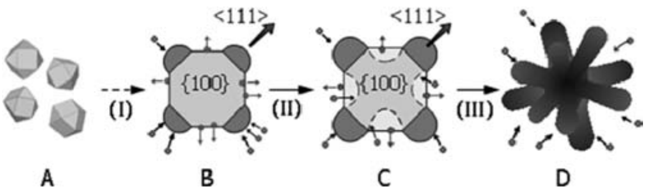

Figure 4. Schematic illustration of the growth mechanism for platinum nanocrystals in the high concentration reaction, through the first three growth stages (I−III). Platinum monomers first (A) nucleate into cuboctahedral nuclei, and then (B) grow into single-crystalline quasi-octapods. Growth of the arms of the quasi-octapods coupled with selective etching on the edges and centers of facets leads to (C) formation of etched-octapods. These processes continue and (D) transform the nanocrystals to porous nanocrystals.

dissolved in the solvent.[36−39] In the present synthesis, halide ions are not present; and the amount of any residual oxygen dissolved in the degassed solvent should be minimal and similar in both low- and high-concentration reactions. As etching is observed only in the high-concentration reaction, it is thus likely that the etchant originates from the acetylacetonate precursor or a byproduct of acetylacetonate. Acetylacetone has been shown to etch the surface of nickel and copper metals with Nigg and co-workers showing that the etchant species was an enol form of acetylacetone and etching occurred via a chelation process.[40,41] A similar mechanism is likely to take place in the etching of the platinum nanoparticles in this study.

Etching most likely commences rather abruptly at ∼100 min in Stage II. At this point in the reaction, enough of the platinum acetylacetonate has reacted to produce a sufficiently high concentration of the etchant to begin etching the nanocrystals. The etching process is possibly taking place all over the nanocrystals. However, TEM data show selective etching on the {100} faces of the quasi-octapods. Selective etching on {100} faces of palladium nanocubes has been previously reported by Xia and co-workers.[26,42] As the {100} facets generally have higher surface energy than surfaces bound by {111} facets, there is higher tendency for the etchant to adsorb to and redissolve the platinum atoms on the {100} facets.[34]

At ∼180 min (end of Stage II), the etching is observed to have stopped and growth continues rapidly. There are two reasons for the end of Stage II growth. First, we observe that etching takes place almost exclusively on the {100} facets. Hence when no {100} facets are available at the end of Stage II, the etching process is retarded and unlikely to occur. Second, when enough atoms on the {100} facets are removed, high-index facets together with kinked and stepped faces are exposed. The newly exposed faces are believed to be the main driving factor for the rapid growth that commences in Stage III. It is known that kinks and steps can induce preferential and spontaneous growth, resulting in much faster growth rates on faces with these defects.[43,44]

Previous studies have shown that oxidative etching on fcc metal nanocrystals preferentially takes place on rounded tips, concave regions, and twin defects.[25,36,37,45] In many cases, this form of selectivity has caused the removal of nanocrystals with irregular shapes, branched structures and twinned nanoparticles by complete dissolution or by conversion into near-spherical and uniform polyhedral nanostructures. In stark contrast, the selective etching observed here leads to multiply branched and porous nanostructures. Importantly, the etching process in the current system is highly facet-selective and occurs relatively briefly during growth (as compared to the duration of experiment). The etching occurs during an early growth stage such that after this process stops rapid nanocrystal growth continues in a kinetically controlled regime. Although different mechanisms have been proposed for the growth of porous platinum nanoparticles,[15,46] in the present case, selective etching has been demonstrated to be the key step.

Conclusions

The growth and evolution of platinum nanocrystals in solutions of different precursor concentrations have been investigated with in situ XRD and ex situ TEM. The low-concentration reaction has been shown to produce faceted and compact morphologies. The growth is shown to be relatively slow and is in a thermodynamically controlled regime. In a reaction with high precursor concentration, branched and porous morphologies are obtained. The growth is more complex and has been shown to be under a kinetically controlled regime. The results and analyses have demonstrated that growth in the high-concentration reaction involved a structural transformation mechanism for octapod-like nanocrystals to grow into porous nanostructures. A new mechanism involving selective growth and etching that occurs during early growth stages has been shown to be responsible for the transformation. This combined set of measurements demonstrates the utility and complementarity of TEM and in situ XRD for revealing the growth details of these complex materials.

These findings are useful in understanding the formation of platinum nanocrystals of different morphologies. Furthermore, it is hoped that the understanding developed will aid in the design of new synthetic methodologies, which are applicable to other fcc metals.

Acknowledgment. Portions of this research were carried out at the Stanford Synchrotron Radiation Lightsource (SSRL), a national user facility operated by Stanford University on behalf of the U.S. Department of Energy, Office of Basic Energy Sciences. We thank the SSRL staff and particularly Valery Borzenets with assistance with the experimental setup at SSRL. R.D.T. thanks the MacDiarmid Institute for funding. S.C. thanks the Marsden Fund IRL-0602 and the Victoria University Science Faculty Research Grant for funding.

Supporting Information Available: Figures S1−S12 (PDF). This material is available free of charge via the Internet at http://pubs.acs.org.

JA9065688

---

(36) Wiley, B.; Herricks, T.; Sun, Y.; Xia, Y. *Nano Lett.* **2004**, *4*, 1733–1739.

(37) Tsung, C.-K.; Kou, X.; Shi, Q.; Zhang, J.; Yeung, M. H.; Wang, J.; Stucky, G. D. *J. Am. Chem. Soc.* **2006**, *128*, 5352–5353.

(38) Grzelczak, M.; Perez-Juste, J.; Mulvaney, P.; Liz-Marzan, L. M. *Chem. Soc. Rev.* **2008**, *37*, 1783–1791.

(39) Lim, B.; Jiang, M.; Tao, J.; Camargo, P. H. C.; Zhu, Y.; Xia, Y. *Adv. Funct. Mater.* **2009**, *19*, 189–200.

(40) Nigg, H. L.; Ford, L. P.; Masel, R. I. *J. Vac. Sci. Technol.* **1998**, *A16*, 3064–3067.

(41) Nigg, H. L.; Masel, R. I. *J. Vac. Sci. Technol.* **1998**, *A16*, 2581–2584.

(42) Xiong, Y.; Xia, Y. *Adv. Mater.* **2007**, *19*, 3385–3391.

(43) Chernov, A. A. *Acta Crystallogr., Sect. A* **1998**, *54*, 859–872.

(44) Henry, C. R. *Prog. Surf. Sci.* **2005**, *80*, 92–116.

(45) Zettsu, N.; McLellan, J. M.; Wiley, B.; Yin, Y.; Li, Z.-Y.; Xia, Y. *Angew. Chem., Int. Ed.* **2006**, *45*, 1288–1292.

(46) Zhang, H.-T.; Ding, J.; Chow, G.-M. *Langmuir* **2008**, *24*, 375–378.